metals

MDPI

Article

Damping and Compressive Properties of SLM-Fabricated Rhombic Dodecahedron-Structured Ni–Ti Shape Memory Alloy Foams

Di Guo [1], Qingzhou Wang [1,*], Li Liu [1], Shuo Liu [1,2], Hao Cao [1], Jingxia Xie [1] and Fuxing Yin [2]

[1] The "Belt and Road Initiative" Advanced Materials International Joint Research Center of Hebei Province, School of Materials Science and Engineering, Hebei University of Technology, Tianjin 300130, China; g1360465113@163.com (D.G.); liuli951007@163.com (L.L.); ls419522@163.com (S.L.); 19969971122@163.com (H.C.); x18403208056@163.com (J.X.)

[2] Institute of New Materials, Guangdong Academy of Sciences, Guangzhou 510651, China; yinfuxing@hebut.edu.cn

* Correspondence: qzwang@hebut.edu.cn

Abstract: Ni–Ti shape memory alloy (SMA) foams, capable of bringing revolutionary changes to crucial fields such as aerospace, energy engineering, and biomedical applications, are at the forefront of materials science research. With the aim of designing Ni–Ti SMA foams with complex structures, near-equiatomic Ni–Ti SMA foams featuring a rhombic dodecahedron (RD) structure were fabricated using selective laser melting (SLM) technology. Damping, superelasticity, and quasi-static compressive mechanical tests were carried out on the resultant foams. The findings indicated that the smaller the unit structure of the RD or the larger the rod diameter, the higher the damping and compressive strength of the foams would be. Foams with a cell structure of 2 mm × 2 mm × 2 mm and a rod diameter of 0.6 mm exhibited the highest damping, reaching up to 0.049, along with the highest compressive strength, reaching up to 145 MPa. Furthermore, if the specimen underwent solution and aging heat treatments, its strength could be further enhanced. Meanwhile, the specimens also exhibited excellent superelasticity; even when the pre-strain was 6%, the elastic recovery could still reach 97%. Based on microstructure characterization and finite element simulation, the property mechanisms and deformation rules of the foams were revealed.

Keywords: additive manufacturing; Ni–Ti SMA foam; microstructure; damping; compressive properties

check for updates

Academic Editor: Gabriel A. Lopez

Received: 17 February 2025
Revised: 15 March 2025
Accepted: 18 March 2025
Published: 19 March 2025

Citation: Guo, D.; Wang, Q.; Liu, L.; Liu, S.; Cao, H.; Xie, J.; Yin, F. Damping and Compressive Properties of SLM-Fabricated Rhombic Dodecahedron-Structured Ni–Ti Shape Memory Alloy Foams. *Metals* **2025**, *15*, 335. https://doi.org/10.3390/met15030335

Copyright: © 2025 by the authors. Licensee MDPI, Basel, Switzerland. This article is an open access article distributed under the terms and conditions of the Creative Commons Attribution (CC BY) license (https://creativecommons.org/licenses/by/4.0/).

1. Introduction

Ni–Ti shape memory alloy (SMA) foams, with their remarkable shape memory effect, outstanding superelasticity, excellent biocompatibility, high damping capacity, and lightweight design, are poised to bring about revolutionary changes in crucial sectors such as aerospace, automotive engineering, and biomedical applications. For instance, Ni–Ti SMA foams are being considered for aircraft structural applications, such as internal wing and fuselage supports. Their unique thermomechanical properties enable dynamic shape adjustment in adaptive wing systems, where temperature or stress actuation optimizes aerodynamic performance during flight. In automotive engineering, these materials show promise in intelligent crash-absorbing bumpers and energy-dissipating seat components that combine superelastic recovery with structural integrity. Biomedical applications leverage both the superelastic behavior of Ni–Ti foams to accommodate physiological motion in

vascular implants and their porous architecture to facilitate tissue ingrowth and osseointegration. Their unique physical and mechanical properties have already led to extensive utilization in these fields, and they continue to be a focus of cutting-edge research [1,2]. As modern technology advances steadily, the need for devices crafted from Ni–Ti SMA foams with complex structures, superior compressive superelasticity, and high-performance energy-absorption capabilities becomes increasingly pressing [3,4]. Many scholars have conducted research on Ni–Ti foam alloys. For example, Lai et al. explored microwave sintering for Ni–Ti foam alloys [5], Guo et al. focused on a new top-down process for high-damping Ni–Ti foam alloys [6], Andani et al. studied the selective laser melting of Ni–Ti foam alloys [7], Li et al. dealt with Ni–Ti-based negative Poisson's ratio structures fabricated by selective laser melting [8], Bertheville et al. reported on single-phase Ni–Ti foam for bone graft applications [9], Salvetr et al. presented an SHS technology for Ni–Ti tubes [10], and Zhu et al. reported metal injection molding for high-performance microporous Ni–Ti foam alloys [11]. It is widely recognized that the preparation and processing of Ni–Ti SMA foams is a highly challenging task, as traditional preparation methods have difficulties in producing structural components with complex configurations.

Recently, additive manufacturing (AM) has presented an opportunity to fabricate metal foams with complex structures. This process enables precise control over hierarchical internal structures, enhancing material utilization and lightweight performance critical for aerospace, biomedical, and automotive applications. However, AM is constrained by limited material options, slower production rates, and higher costs compared to conventional methods. Despite these challenges, AM remains essential for applications requiring intricate geometries unattainable via traditional manufacturing [12–14]. Among these, selective laser melting (SLM) technology enables the rapid production of precise, small, and/or medium-sized parts, thereby rendering it a more efficient and high-quality approach for preparing foam structures [15,16].

In recent years, honeycomb materials, as a particular type of metal foams, have drawn significant attention due to their lightweight and high-strength characteristics, heat and sound insulation properties, energy absorption and shock absorption capabilities, as well as excellent dimensional stability [17,18]. Honeycomb materials can be categorized into random topological structures and periodic topological structures, with periodic honeycomb materials mainly encompassing two-dimensional and three-dimensional dot matrix materials [19]. Honeycomb materials with RD periodic topology are regarded as having higher compressive mechanical properties and more effective energy absorption properties [20–22].

Xiao et al. investigated the compressive behavior of Ti-6Al-V alloys with an RD structure at four different strain rates and discovered that the peak stress is dependent on the loading rate for structures with small unit cells [23]. Xiao et al. also examined the deformation modes along with the compressive properties of Ti-6Al-V alloys with an RD structure at different temperatures and revealed their evolutionary patterns [24]. Babaee et al. investigated the mechanical properties of the RD structure and demonstrated that this lattice structure is an incompressible structure with orthogonal anisotropy and that the material properties are mainly determined by the bending of the cell edges [25]. Babamiri et al. investigated nickel-based high-temperature alloys with an RD structure and disclosed the mechanisms of their stress–strain response and energy absorption properties [26]. Epasto et al. investigated the mechanical behavior of RD structures under compression and low-velocity impact loading and found that small-sized cell structures are more suitable for impact protection [27]. Yang et al. demonstrated that an increase in the RD cell size (RDCS) leads to a decrease in the Young's modulus, yield strength, and energy-absorbing capacity [28]. Cao et al. examined the mechanical response and

energy-absorbing properties of RD structures in quasi-static and dynamic compression experiments. The results indicated that the RD structures exhibited persistent and stable post-yield responses at different loading rates, which ensures minimized stress transfer under strong impacts [29,30].

Numerous scholars have delved into the compression/energy absorption characteristics of foam metals with an RD structure. However, to date, the research on Ni–Ti SMA foams with an RD structure prepared using the SLM technique remains inadequate, particularly as few have systematically investigated the damping property of this material (where damping represents the energy absorption property within the elastic deformation range). In order to furnish the theoretical basis and technical support for the research and development of Ni–Ti SMA foams with excellent, comprehensive properties and to promote the widespread application of this material, the damping and compression mechanical properties of Ni–Ti SMA foams with an RD structure prepared using the SLM technique were studied, and the associated mechanisms were discussed. Moreover, in the SLM of Ni–Ti SMA foams, the choice between pre-alloyed Ni–Ti powders and elemental Ni–Ti powder mixtures significantly influences the processing behavior and final material properties. Elemental powders offer cost advantages and compositional flexibility, but their differing melting points (Ni: 1455 °C vs. Ti: 1668 °C) and reaction kinetics under laser irradiation pose challenges in achieving uniform melt pools and stoichiometric control [31]. This non-uniformity often results in residual porosity and incomplete intermetallic reactions. Intriguingly, residual microporosity within pore walls has been found to enhance the damping properties [32]. Conversely, pre-alloyed Ni–Ti powders facilitate the formation of homogeneous melt pools that solidify rapidly into austenite matrices, leading to denser pore walls. The present study employs elemental Ni–Ti powders to reduce manufacturing costs while maintaining material functionality, providing critical insights for optimizing the SLM process parameters of functional Ni–Ti SMA foam components.

2. Materials and Methods

$Ni_{50.7}Ti_{49.3}$ SMA foams with an RD structure were fabricated using pure Ni and Ti powders (CHINA, with a purity of 99.9% and an average powder size ranging from 20 to 50 μm) as raw materials via SLM on a 3D printer (EOS M290, Krailling, Germany). To achieve superelasticity at room temperature, the content of Ni was deliberately increased on the basis of the near-equiatomic ratio of Ni–Ti. The chemical composition of the mixed Ni–Ti powders is presented in Table 1. The printing process parameters were set as follows: a laser power of 150 W, a scanning speed of 1100 mm/s, a scanning spacing of 0.1 mm, an interlayer scanning direction rotation angle of 67°, and a layer thickness of 40 μm. The specifications of the specimens prepared in this study are presented in Table 2. The overall size of the columnar specimens was Φ30 mm × 30 mm. The structural model of the RD cell and the SLM principle are illustrated in Figure 1. The relative density was measured using the Archimedes method:$\boldsymbol{\rho_r = \rho_e/\rho_t}$, where $\boldsymbol{\rho_e}$ is the apparent density and $\boldsymbol{\rho_t}$ is the theoretical density of 6.50 g/cm^3. The porosity was then obtained from $\boldsymbol{\eta = 1 - \rho_r}$. The specimens underwent solid solution treatment at 1000 °C, followed by aging. The aging treatment was carried out at 350 °C for 0.5 h, 1 h, 1.5 h, and at 450 °C for 1 h. The specimens used for microscopic observation were polished using sandpaper, step by step, and then polished with diamond polishing paste with a grain size of 0.5 μm. The specimens were then immersed in an etching solution with a ratio of HF:HNO_3:H_2O of 1:1:5 for 8–10 s. The microstructures were observed by means of a scanning electron microscope (SEM, JSM-6510A, Tokyo, Japan). The elemental distribution was detected using an electron probe microanalyzer (EPMA, JEOL 8530F, Tokyo, Japan). The crystal orientation, grain size, and dislocation density were analyzed using electron backscatter diffraction (EBSD, EDAX

Velocity Super, Berwyn, PA, USA). For EBSD analysis, a 2 kV argon ion-beam polishing system (Gatan PIPS Pro, Pleasanton, CA, USA) was used to polish the prepared surface for 15 min. This process aimed to eliminate mechanical damage while preserving the porous structure. Etching was performed using a solution of 3% HF, 10% HNO_3, and 87% H_2O for 10 s to reveal grain boundaries. This protocol ensures optimal contrast for the EBSD indexing of Ni–Ti foam microstructures. Phase analysis was performed on an X-ray diffractometer (XRD, Bruker D8 Discover, Berlin, Germany) using Cu Kα radiation. The set parameters are as follows: scanning speed 6°/min, scanning range 10–90°, and power 4 kW. The phase transformation curves of the specimens were obtained with a differential scanning calorimeter (DSC, Q20). The damping was tested on a dynamic mechanical analyzer (DMA, Q800) within the temperature range of −50 °C to 150 °C at a heating rate of 3 °C/min. Quasi-static compression tests were conducted on a universal testing machine (UTM, Instaron, Norwood, MA, USA) with a strain rate of 1 mm/min. The superelasticity was evaluated in the form of stress loading–unloading. The damping test specimens had dimensions of 30 mm × 10 mm × 2 mm, and cylindrical specimens of Φ10 mm × 15 mm were used for the quasi-static compression and superelasticity tests. The deformation rule of the specimens and the associated mechanisms were simulated using the ABAQUS software (version 2022).

Table 1. Chemical composition of the mixed Ni–Ti powders.

Element	Ti	Ni	Fe	C	O	N
Content (wt.%)	44.17	55.74	0.010	0.009	0.060	0.011

Table 2. Specification of specimens.

Specimen Number	**RDCS (x y z)**	**Rod Diameter (mm)**
1#	2 mm × 2 mm × 2 mm	0.2
2#	2 mm × 2 mm × 2 mm	0.4
3#	2 mm × 2 mm × 2 mm	0.6
4#	3 mm × 3 mm × 3 mm	0.2
5#	3 mm × 3 mm × 3 mm	0.4
6#	3 mm × 3 mm × 3 mm	0.6

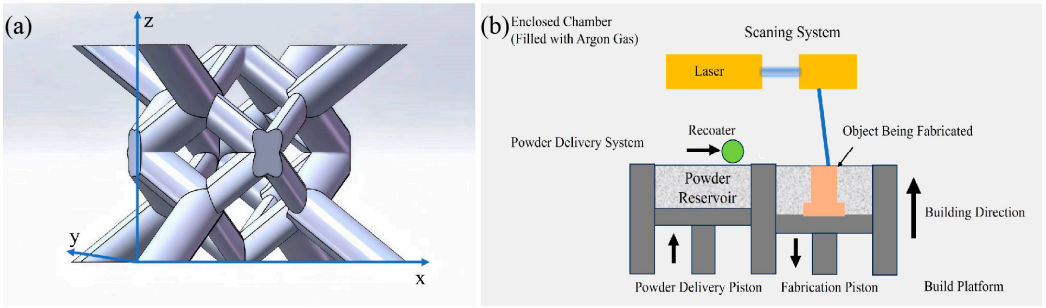

Figure 1. Schematic diagrams of (**a**) the RD cell and (**b**) the SLM principle.

3. Results and Discussion

3.1. Characterization of Macroscopic Morphologies and Microstructures

Figure 2 presents the macroscopic and microscopic morphologies of the SLM specimens with different parameters. It can be observed that the SLM method exhibits a high level of controlling precision over the dot matrix structure of the Ni–Ti SMA foam. However, a small quantity of adhesive powder is present on the surface of the component stubs. This is attributed to the fact that when the laser scans the structural contour,

the surrounding area of the molten pool partially melts due to the high temperature, causing the powder to adhere to the outer edge of the stubs. No evident defects such as cracks or holes can be detected, and the size of the rod diameter varies significantly with different parameters.

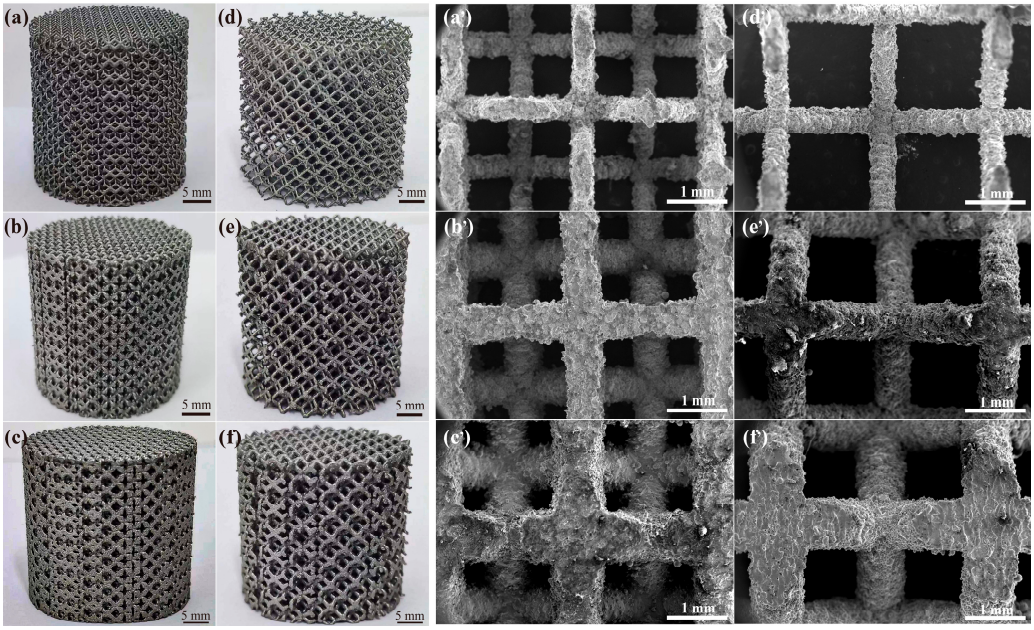

Figure 2. Images (**a**–**f**) show the macro and (**a′**–**f′**) micro morphologies of $1^{\#}$–$6^{\#}$ specimens.

Figure 3 depicts the microstructure of the SLM-manufactured Ni–Ti SMA with different structural parameters. It can be noticed that the specimens are predominantly composed of lamellar and fine stripe-like microstructures. Moreover, at the same RDCS (rhombic dodecahedron cell size), the larger the rod diameter, the finer the microstructure. Conversely, at the same rod diameter, the larger the RDCS, the coarser the microstructures.

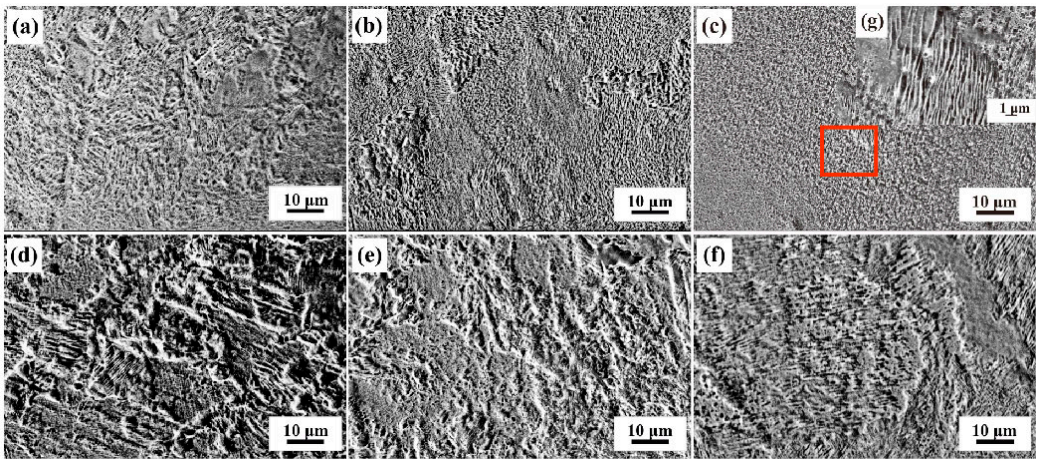

Figure 3. Microstructures of (**a**) $1^{\#}$, (**b**) $2^{\#}$, (**c**) $3^{\#}$, (**d**) $4^{\#}$, (**e**) $5^{\#}$, (**f**) $6^{\#}$ specimens; (**g**) enlarged view of the region within the red box in (**c**).

Figure 4 depicts the microstructures of the $3^{\#}$ specimen after heat treatments. Given the near-equiatomic composition of the specimen (close to 1:1), after solution and aging treatments, the matrix predominantly consists of the B2 austenite phase at room temperature. Evidently, precipitates also emerge and are predominantly distributed at the grain boundaries upon aging. The size of these precipitates gradually increases with the increase in either the aging temperature or the aging time. Comparing the EDS results shown in

Figure 5 and the XRD results in Figure 6 with the precipitates in the SEM images, it can be determined that these precipitates are Ti_2Ni phases [33,34].

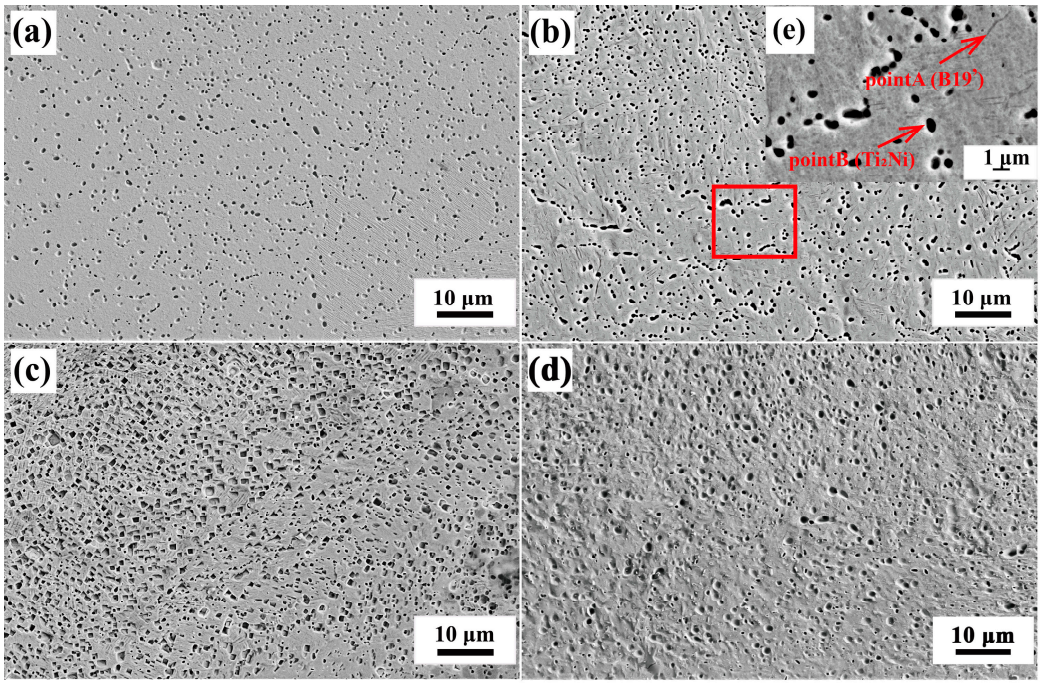

Figure 4. Microstructures of 3# specimen after solution and aging (**a**) at 350 °C for 0.5 h, (**b**) at 350 °C for 1 h, (**c**) at 350 °C for 1.5 h, (**d**) at 450 °C for 1 h; (**e**) enlarged view of the region within the red box.

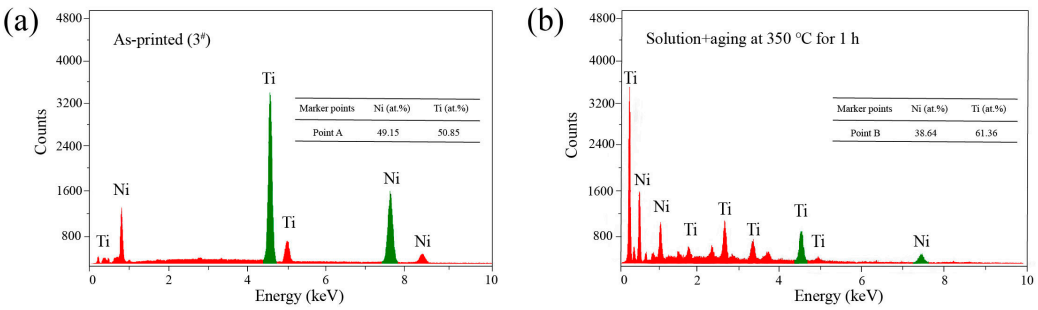

Figure 5. EDS analysis results of point A (**a**) and point B (**b**) shown in Figure 4b.

The XRD results presented in Figure 6 indicate that the as-printed 3# specimen primarily comprises the B2 austenite phase, accompanied by minor fractions of the B19′ martensite and Ti_2Ni phase. These phases can be seen in Figures 3 and 4 as lamellar austenite, finely striated martensite, and spherical Ti_2Ni particles, respectively [33,34]. The phase composition of the Ni–Ti SMA foam undergoes significant changes after heat treatments. After solid solution treatment and aging at 450 °C for 1 h, the intensity of the diffraction peak of the B2 phase decreases, whereas the intensity of the diffraction peak of the B19′ phase increases, and a small amount of Ni_3Ti phase and Ni_4Ti_3 phase emerge. After solid solution treatment and aging at 350 °C for 0.5 h, the intensity of the diffraction peak of the B19′ phase increases. The Ni_4Ti_3 phase also emerges, and as the aging time is extended, the intensities of the diffraction peaks of both the Ni_4Ti_3 and Ti_2Ni phases increase [35]. According to the literature [36], the Ni_4Ti_3 phase grows as the aging temperature rises and the aging time lengthens, with its area proportion capable of reaching 20–30%.

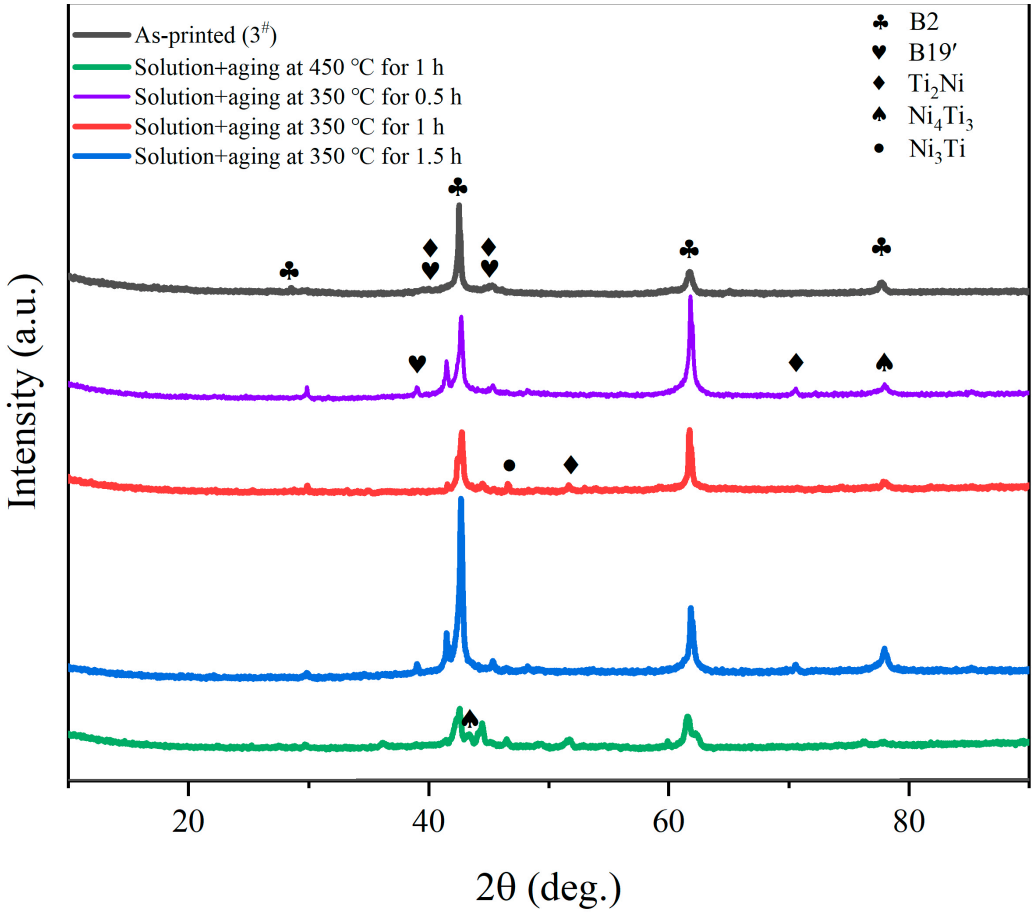

Figure 6. XRD patterns of 3# specimens in different heat treatment states.

EBSD characterization was carried out to disclose more details regarding the microstructural changes before and after heat treatments. From Figure 7a,d, it can be noticed that the proportion of low-angle grain boundaries rises from 0.29 to 0.51 after heat treatments, which might be attributed to the formation of interfaces between the R and B2 phases. It has previously been reported that a stress mismatch exists between the R and B2 phases, and this mismatch causes dislocations at the interface; the generation and movement of these dislocations facilitate the formation and migration of grain boundaries, thus increasing the number of small-angle boundaries [37,38]. From Figure 7b,e, it is clear that most of the grains are colored red. The specimen has a texture with a preferred orientation along the [001] direction, and the intensity of the texture increases from 3.670 to 6.574 after heat treatments. A comparison between Figure 7c,f reveals the increase in dislocation density after heat treatments. The increase in dislocation density can be ascribed to the thermal stresses induced by water cooling after solid solution treatment, as well as the presence of a stress field around the precipitated phases. Figure 8 depicts the grain size of the 3# specimen before and after heat treatments. The standard deviations are 13.878 and 16.482, respectively. It can be seen that the average grain size increases slightly after heat treatments.

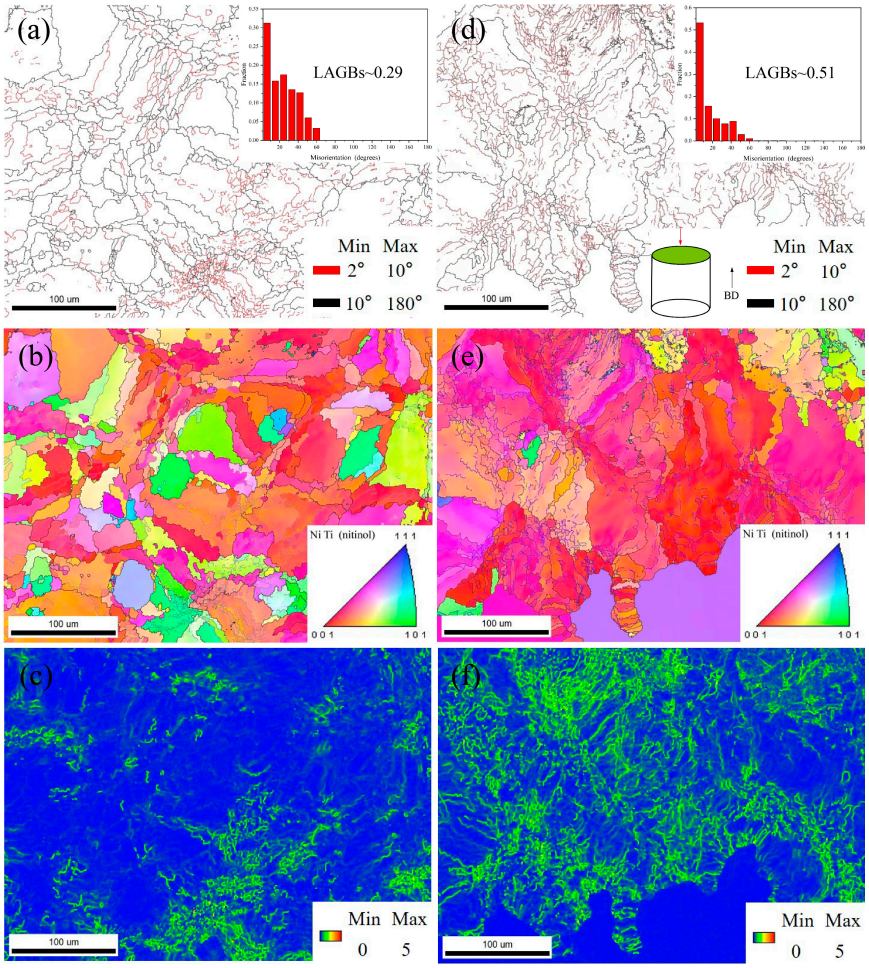

Figure 7. Images (**a**–**c**) and (**d**–**f**) represent the grain boundary distribution, inverse pole figure (IPF), and kernel average misorientation (KAM) of the 3# specimens before and after heat treatment (solid solution treatment + aging at 350 °C for 1 h), respectively.

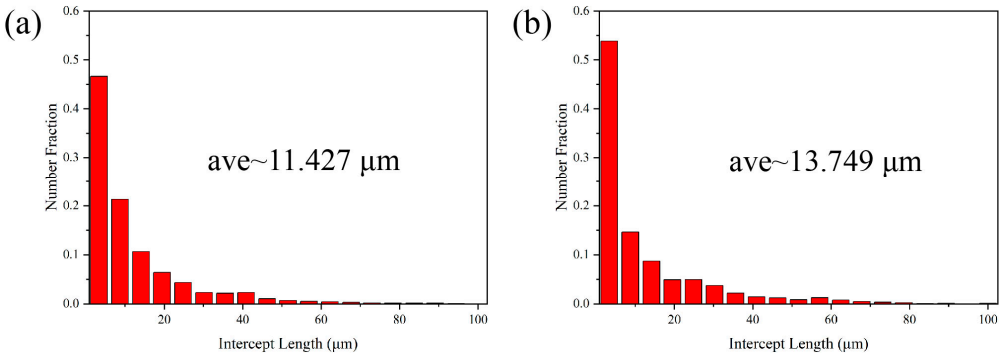

Figure 8. Average grain size of 3# specimen (**a**) before and (**b**) after heat treatments (solution + aging at 350 °C for 1 h).

3.2. Property Tests and Mechanism Analysis

Figure 9 presents the thermal analysis results of the 3# specimen before and after heat treatments. It can be observed that the as-printed 3# specimen displays a one-step phase transformation of B19′ → B2 during the heating process, with only one endothermic peak P1 emerging. Conversely, a single exothermic peak P2 appears during cooling, which is attributed to the one-step B2 → B19′ phase transformation. Significant changes take place after heat treatments: the phase transformation characteristic temperatures shift

toward the high temperature side, and a two-step phase transformation occurs during the heating process. The first endothermic peak P3 corresponds to the transformation of B19′ → R, and the second endothermic peak P4 corresponds to the transformation of R→B2. However, only a single exothermic peak P5 emerges during cooling, corresponding to the one-step B2 → B19′ phase transformation. The two-step transformation during the heating process can be attributed to the fact that the obstructive effect of the Ni_4Ti_3 phase precipitated during aging on the B2 → B19′ transformation is much stronger than that on the B2 → R transformation, due to the considerably larger transition strain of the former [39]. The precipitation of the Ni-rich precipitated phase in the matrix during the aging treatment results in a decrease in the Ni content in the matrix, thereby increasing the phase transformation temperatures. Notably, according to the binary alloy phase diagram of Ni–Ti, both the Ti_2Ni and Ni_4Ti_3 phases remain stable within the temperature range of the DSC test. This means that the presence of these two phases has no influence on the appearance of the peaks in the DSC curves.

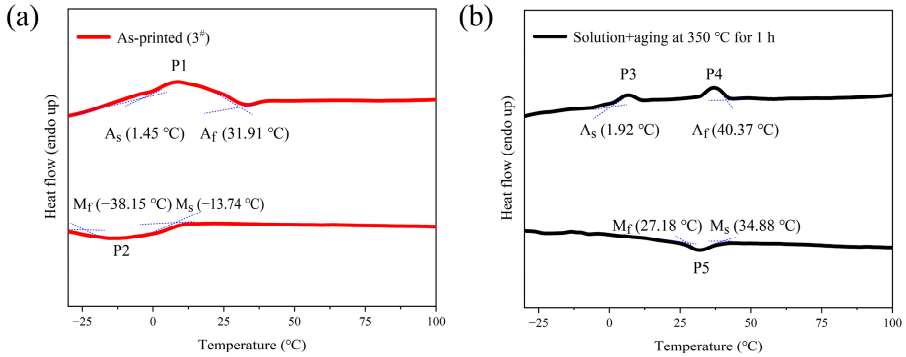

Figure 9. DSC results of 3# specimen (**a**) before and (**b**) after heat treatments (solution + aging at 350 °C for 1 h).

The damping behaviors of Ni–Ti SMA foams during heating are depicted in Figure 10. The damping curves of the 1# and 4# specimens are not presented as their damping data were unreliable; this is because they experienced deformation under the clamping action of the fixture during damping testing using DMA due to their thin rod diameter. From Figure 10a, it is observed that a damping peak emerges. From Figure 10b,c, it is evident that this damping peak increases with a decrease in the measuring frequency or an increase in the heating rate, exhibiting a typical characteristic of first-order phase transformation [39]. In combination with the DSC result shown in Figure 9a, it can be determined that this damping peak originates from the reverse martensitic phase transformation. From Figure 10a, it can also be noticed that the damping approximately increases with the decrease in RDCS (rhombic dodecahedron cell size) or the increase in rod diameter. This is because the high damping of Ni–Ti SMA foams mainly originates from the inherent damping of the Ni–Ti matrix. Although pores also have a damping effect, the relative content of the Ni–Ti matrix should be the dominant factor for the damping peak arising from the phase transformation from martensite to austenite. Figure 10d shows the damping of the 3# specimen in different states. It can be seen that the damping of the specimen significantly decreases after heat treatments, which is related to the appearance of precipitated phases during the aging process. These precipitated phases can effectively pin various phase interfaces, reducing their mobility and thus lowering their energy dissipation capacity. At 350 °C, as the aging time increases, the damping first increases and then decreases. This is because when the aging time is relatively short, the precipitated phases are small and dispersed [40], so their pinning effect on various phase interfaces is the strongest. As the aging time prolongs, the precipitated phases gradually grow and are inhomogeneously distributed [41]. In some

areas, the pinning force on the phase interfaces decreases, resulting in a slight increase in damping. However, as the aging time continues to prolong, the amount of precipitated phases increases significantly, which further leads to a decrease in damping.

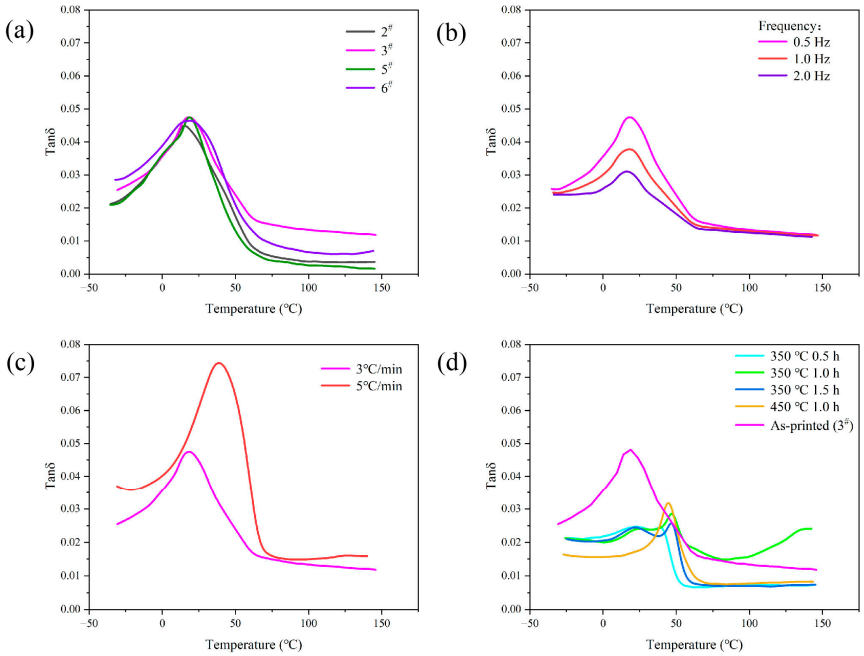

Figure 10. Damping behaviors of Ni–Ti SMA foams: (**a**) as-printed $2^{\#}$, $3^{\#}$, $5^{\#}$, and $6^{\#}$ specimens; (**b**) effect of measuring frequency on the damping behavior of $3^{\#}$ specimen; (**c**) effect of heating rate on the damping behavior of $3^{\#}$ specimen; (**d**) damping behavior of $3^{\#}$ specimen in different states.

After aging at 350 °C, the phase transformation damping peak during the heating process is divided into two, which is related to the two-step phase transformation caused by the Ni_4Ti_3 phase mentioned earlier: B19′ → R and R → B2 each produce a damping peak. After aging at 450 °C, the damping further decreases, which is related to the significant decrease in the Ni–Ti phase content after aging at this temperature. The disappearance of the two-step phase transformation phenomenon can be attributed to the gradual growth of the Ni_4Ti_3 phase due to the increase in aging temperature, resulting in a weakening of the coherency between the Ni_4Ti_3 phase and the matrix, and thus a weakening of the obstructive effect on the B2 → B19′ transformation [42]. Figure 11 illustrates the damping behavior of the $3^{\#}$ specimen, which was measured using a stepwise heating approach. The heating rate was set at 3 °C/min. Specifically, after each increment of 10 °C in temperature, the heating process was paused, and the temperature was held constant. After maintaining this temperature for 15 min, the damping value was measured. Subsequently, the heating was resumed. From Figure 11, it can be seen that the difference in damping before and after heat treatments measured by the isothermal method is significantly reduced. The phase transformation damping peak is mainly composed of three parts: $Q_{tot}^{-1} = Q_{tr}^{-1} + Q_{pt}^{-1} + Q_{int}^{-1}$, where Q_{tr}^{-1} represents the transient damping that acts only during continuous heating or cooling, Q_{pt}^{-1} is related to the phase transformation, and Q_{int}^{-1} comes from the contribution of each phase [43,44]. During isothermal testing, the first part of the transient damping essentially vanishes, thus leading to a significant decrease in the high damping peak of the specimen prior to heat treatments. As is commonly known, damping materials are typically employed under isothermal conditions. Consequently, the heat treatments do not significantly reduce the energy dissipation capacity of the Ni–Ti foams.

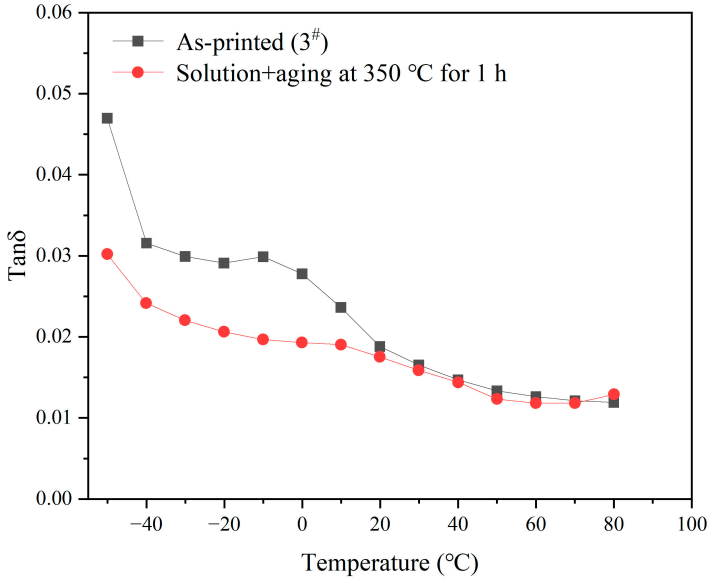

Figure 11. Damping as a function of temperature during step heating (heating rate 3 °C/min, heating step 10 °C with holding time 15 min).

Figure 12a depicts the compressive stress–strain curves of Ni–Ti SMA foams. It can be observed that, for the same RDCS, the compressive strength gradually increases as the rod diameter grows. When the rod diameter remains constant, the smaller the RDCS, the higher the compressive strength. This is consistent with the regulatory mechanisms of structural parameters on strength reported by Engene et al. and Han et al. [45,46]. Specifically, the compressive strength of specimen 3# can reach 145 MPa. Additionally, the figure shows that the stress–strain curves of all specimens follow a similar pattern of variation. Initially, in stage I, there is elastic deformation of the austenite phase. This is then succeeded by stress-induced martensitic transformation in stage II. During this stage, the rate at which stress increases with strain decelerates. Once the stress-induced martensitic transformation is complete, the single-phase martensite deformation stage (stage III) commences. Subsequently, as the strain continues to rise, the pore walls of the specimens start to experience severe plastic deformation, ultimately leading to pore collapse and specimen fracture. As is evident from Figure 12a, specimen 3# demonstrates the highest quasi-static compressive mechanical properties (with a compressive strength of 145 MPa and an elongation of 15%). Figure 12b,c illustrate the superelasticity of specimen 3# before and after heat treatment under various pre-strains. Clearly, the pre-strain of specimen 3# can reach up to 10% (when the pre-strain exceeds 10%, the pores in the specimen begin to collapse, making the specimen unfit for superelasticity testing). However, the pre-strain of the heat-treated specimen is restricted to 6%. Significantly, after the heat treatment of specimen 3#, the stress of the stress-induced martensitic transformation increases from 61 MPa to 85 MPa. Also, at a pre-strain of 6%, the maximum stress value of specimen 3# rises from 89 MPa before heat treatment to 132 MPa after heat treatment. Upon stress removal, the elastic recovery of the heat-treated specimen 3# can reach 5.80% (with an elastic recovery rate of 97%). In comparison, under the same pre-strain, the elastic recovery of the specimen before heat treatment is merely 4.75% (with an elastic recovery rate of 79%). Evidently, heat treatment significantly enhances the superelasticity of the specimen. This is mainly attributed to the formation of Ni_4Ti_3 and Ti_2Ni precipitates after heat treatment. These precipitates can effectively impede the dislocation motion and increase the critical slip stress of the matrix [32]. As a result, the plastic deformation of both the austenite and martensite phases is effectively inhibited, thus improving the superelasticity [47,48]. In fact, Ni–Ti shape memory alloys have excellent shape memory properties. For instance,

Girolamo studied the effect of temperature on the mechanical behavior of Ni–Ti shape memory sheets, and found that the shape memory effect was evident at 40 °C, but the best recovery was at 60 °C for some samples [49].

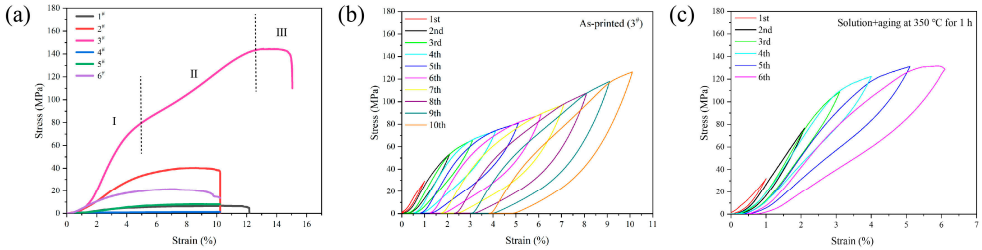

Figure 12. (**a**) Quasi-static compressive stress–strain curves of various specimens; superelasticity of (**b**) specimen 3# and (**c**) heat treated specimen 3#.

Figure 13 shows the changes in macroscopic and microscopic morphologies of the 3# specimen under different strains during compression. As the strain increases, residual strain accumulates, and the overall height of the specimen gradually decreases. Notably, when the deformation reaches 3% and 8% (the stress–strain curve shown in Figure 12 indicates the stress-induced martensite transformation stage), the specimen demonstrates reversible deformation: macroscopic height recovery occurs upon stress removal, and no significant microstructural changes are observed in the pore morphology. However, when the strain reaches 12%, the stress–strain curve enters the single-phase martensite deformation stage, and fracture will occur soon afterwards. At this critical point, irreversible plastic deformation dominates; macroscopic observations reveal permanent height reduction after stress removal, while microscopic observations indicate crack initiation at rod junctions and around pore walls.

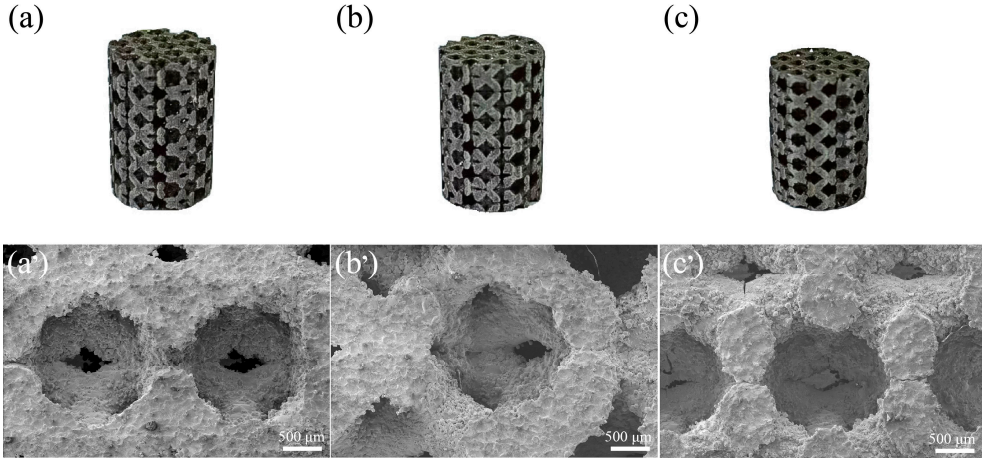

Figure 13. Images (**a**–**c**) show the macroscopic and (**a′**–**c′**) microscopic morphologies of 3# specimen at compressive strains of 3%, 8% and 12%.

In order to disclose the deformation rule and mechanism of Ni–Ti SMA foams during quasi-static compression, ABAQUS software was utilized to simulate the compression process of the 3# specimen. Figure 14 shows the RD structure of the specimen, and the distribution of stress and strain as well as the deformation rule of the 3# specimen during compression are presented in Figure 15. The numerical simulations were conducted using ABAQUS/Standard with an elastic-perfectly plastic constitutive model incorporating experimentally measured material properties, i.e., a density of 6.45 g/cm^3, elastic modulus of 6.2 GPa (Figure 12), yield strength of 145 MPa (Figure 12), and Poisson's ratio of 0.33. A quasi-static compression analysis was performed under displacement-controlled loading,

with the bottom surface fully fixed and the top surface loaded at 1 mm/min. Symmetry boundary conditions were applied to lateral faces to reduce computational cost while maintaining accuracy. The model utilized C3D10 tetrahedral elements with quadratic displacement formulation, discretized at a 0.5 mm element size, validated via a mesh convergence study. Contact interactions between the indenter and specimen were modeled using the penalty method with a friction coefficient of $\mu = 0.02$. Validation against experimental stress–strain curves (Figure 12) revealed excellent agreement, with the maximum deviation in peak stress under 1%. It can be found from Figure 15 that when the compression deformation is 3%, stress can spread throughout the entire specimen, but it is not uniformly distributed and concentrates at nodes with sharp corners. As the compression deformation continues to increase, the stress concentration at the nodes becomes more severe, and the stress in the rods also increases significantly. At this stage, the specimen undergoes internal stress-induced martensitic phase transformation, martensitic selective orientation rearrangement, and dislocation slip. When the strain reaches 12%, the specimen fractures at the node at a 45° angle to the pressure. It can be seen that the simulated deformation rule of the specimen is consistent with the stress–strain curves and the morphology of the compressed specimen shown in Figure 13. Afterwards, the specimen will undergo lateral deformation in its middle part. When the strain exceeds 25%, due to the continued fracture of nodes and the collapse of pores, the specimen begins to lose material in the form of debris falling off. From the strain nephogram, it can be seen that the specimen exhibits a deformation mechanism of layer-by-layer collapse during compression before fracture. When the fragile upper layer of pores collapses and the pore walls fold, high stress will be transmitted to the next layer of pores, causing them to gradually deform and collapse until the specimen fractures. Notably, the data from quasi-static compression experiments were employed as parameters in conjunction with ABAQUS for simulation. In this process, the specific phase composition of the alloy was not taken into account. The simulation results were in good agreement with the actual deformation behavior of the specimens, demonstrating the validity of the simulation. The simulation helped to uncover the laws governing the changes in stress and strain distribution during the compression process, which is conducive to a better understanding of the deformation mechanism.

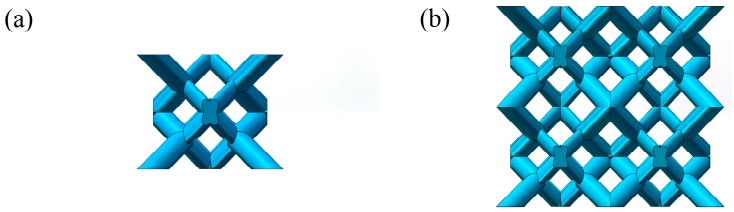

Figure 14. (**a**) RD cell structure; (**b**) dot matrix structure of $3^{\#}$ specimen.

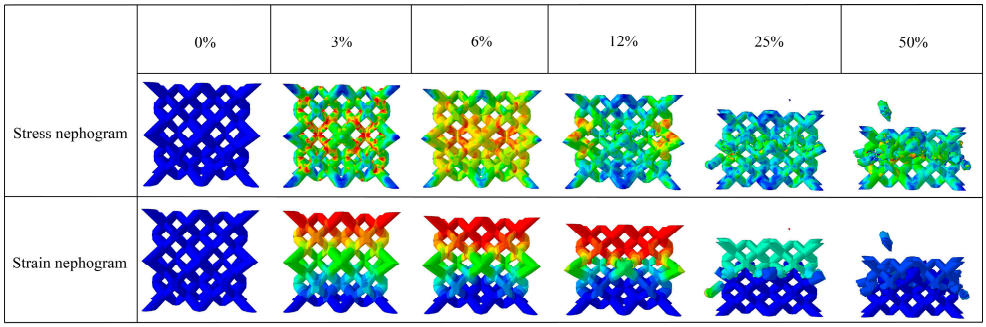

Figure 15. Distribution of stress and strain as well as deformation rule of $3^{\#}$ specimen during quasi-static compression.

4. Conclusions

Ni–Ti SMA foams with different structural parameters were fabricated using the SLM method, and their microstructures, damping, and compressive mechanical properties were investigated. The main findings are as follows:

A larger rod diameter or smaller RDCS results in a finer microstructure of Ni–Ti SMA foams. After solid solution treatment at 1000 °C and aging at 350 °C, Ni_4Ti_3 and Ti_2Ni phases precipitate in the Ni–Ti matrix. As the aging time increases, the size and content of these precipitates grow. A higher Ni_4Ti_3 content relative to Ti_2Ni reduces the Ni content in the matrix, shifting the Ni–Ti phase-transformation temperature to higher values. Moreover, the Ni_4Ti_3 phase increases the nucleation barrier for the B19′ → B2 transition, changing the heating process from a one-step B19′ → B2 to a two-step B19′ → R → B2 phase transformation.

The damping of the as-printed Ni–Ti SMA foams increases with a decrease in RDCS or an increase in rod diameter. When the RDCS is 2 mm × 2 mm × 2 mm and the rod diameter is 0.6 mm, the overall damping is nearly at its maximum. After solid solution treatment at 1000 °C and aging at 350 °C, the damping decreases significantly due to the pinning effect of precipitates. However, two damping peaks appear during heating because of the Ni_4Ti_3-induced two-step phase transformation. After aging at 450 °C, the two-step phase-transformation phenomenon disappears. This is because the increase in aging temperature causes the Ni_4Ti_3 phase to grow gradually, weakening its coherency with the matrix and its obstructive effect on the B2 → B19′ transformation. Under isothermal testing, heat treatment has little effect on damping.

The quasi-static compressive properties of as-printed Ni–Ti SMA foams are enhanced by a smaller RDCS or a larger rod diameter. The specimen with an RDCS of 2 mm × 2 mm × 2 mm and a rod diameter of 0.6 mm has the highest quasi-static compressive mechanical properties (with a compressive strength of 145 MPa and an elongation of 15%). Superelasticity tests indicate that after undergoing solid solution treatment at 1000 °C followed by aging at 350 °C, the maximum pre-strain of specimen $3^{\#}$ decreases from 10% to 6%. However, the superelastic recovery capacity is improved. This is attributed to the precipitation-strengthening effect of the Ni_4Ti_3 and Ti_2Ni phases on both the austenite and martensite phases. For example, at a 6% pre-strain, the elastic recovery rate rises from 79% to 97%.

Author Contributions: Conceptualization, Q.W.; methodology, Q.W. and H.C.; software, L.L.; validation, L.L.; investigation, D.G., L.L., S.L., H.C. and J.X.; resources, F.Y.; data curation, D.G., S.L. and J.X.; writing—original draft preparation, D.G.; writing—review and editing, F.Y.; visualization, S.L.; project administration, Q.W.; funding acquisition, Q.W. All authors have read and agreed to the published version of the manuscript.

Funding: This work was supported by the Natural Science Foundation of Hebei Province (No. E2024202209) and the National Natural Science Foundation of China (No. 52061038).

Data Availability Statement: The raw/processed data required to reproduce these findings cannot be shared at this time due to technical or time limitations. After acceptance, the raw/processed data can be available on request.

Conflicts of Interest: The authors declare that they have no known competing financial interests or personal relationships that could have appeared to influence the work reported in this paper.

References

1. Xu, B.; Yu, C.; Wang, C.; Kan, Q.H.; Wang, Q.Y.; Kang, G.Z. Effect of pore on the deformation behaviors of NiTi shape memory alloys: A crystal-plasticity-based phase field modeling. *Int. J. Plast.* **2024**, *175*, 103931. [CrossRef]
2. Hu, L.; Shen, Z.Y.; Chen, X.J.; Hu, K.Y.; Tang, M.; Wang, L. Microstructure characteristics of porous NiTi shape memory alloy synthesized by powder metallurgy during compressive deformation at room temperature. *Metals* **2023**, *13*, 1806. [CrossRef]
3. Zhang, Y.T.; Wei, D.X.; Chen, Y.; Xie, L.C.; Wang, L.Q.; Zhang, L.C.; Lu, W.J.; Chen, G. Non-negligible role of gradient porous structure in superelasticity deterioration and improvement of NiTi shape memory alloys. *J. Mater. Sci. Technol.* **2024**, *186*, 48–63. [CrossRef]
4. Sun, L.Q.; Chen, K.Y.; Geng, P.; Zhou, Y.; Wen, S.F.; Shi, Y.S. Mechanical and shape memory properties of NiTi triply periodic minimal surface structures fabricated by laser powder bed fusion. *J. Manuf. Process.* **2023**, *101*, 1091–1100. [CrossRef]
5. Lai, T.; Xu, J.L.; Xiao, Q.F.; Tong, Y.X.; Huang, J.; Zhang, J.P.; Luo, J.M.; Liu, Y. Preparation and characterization of porous NiTi alloys synthesized by microwave sintering using Mg space holder. *Trans. Nonferrous Met. Soc. China* **2021**, *31*, 485–498. [CrossRef]
6. Guo, W.; Kato, H. Submicron-porous NiTi and NiTiNb shape memory alloys with high damping capacity fabricated by a new top-down process. *Mater. Des.* **2015**, *78*, 74–79. [CrossRef]
7. Andani, M.T.; Saedi, S.; Turabi, A.S.; Karamooz, M.R.; Haberland, C.; Karaca, H.E.; Elahinia, M. Mechanical and shape memory properties of porous $Ni_{50.1}Ti_{49.9}$ alloys manufactured by selective laser melting. *J. Mech. Behav. Biomed. Mater.* **2017**, *68*, 224–231. [CrossRef]
8. Li, S.; Hassanin, H.; Attallah, M.M.; Adkins, N.J.E.; Essa, K. The development of TiNi-based negative Poisson's ratio structure using selective laser melting. *Acta Mater.* **2016**, *105*, 75–83. [CrossRef]
9. Bertheville, B. Porous single-phase Ni-Ti processed under Ca reducing vapor for use as a bone graft substitute. *Biomaterials* **2006**, *27*, 1246–1250. [CrossRef]
10. Salvetr, P.; Pecenová, Z.; Školáková, A.; Novák, P. Innovative technology for preparation of seamless nitinol tubes using SHS without forming. *Metall. Mater. Trans. A* **2017**, *48*, 1524–1527. [CrossRef]
11. Zhu, B.; Li, D.Y.; Du, C.H.; Wan, Z.C.; Zhou, Y.; Shu, C.; Luo, F.H.; Li, Y.M. Near-spherical micron-porous NiTi alloys with high performances fabricated via metal injection molding. *Mater. Sci. Eng. A* **2024**, *892*, 146114. [CrossRef]
12. Meng, J.; Qiao, Y.; Chen, Y.; Liu, T.W.; Li, T.; Wang, H.Y.; Dai, L.H. A high-entropy alloy syntactic foam with exceptional cryogenic and dynamic properties. *Mater. Sci. Eng. A* **2023**, *876*, 145146. [CrossRef]
13. Liu, J.A.; Liu, S.J.; Wang, B.; Sun, W.B.; Liu, X.J.; Han, Z.W. Compressive property and energy absorption characteristic of interconnected porous Mg-Zn-Y alloys with adjusting Y addition. *J. Magnes. Alloys* **2024**, *12*, 171–185. [CrossRef]
14. Dmimitrova, R.; Simeonova, T.; Krastev, B.; Velikov, A.; Petkov, V.; Manolov, V. Al and A356 alloy foam castings modified with low concentrations of nano-aized particles: Structural study and compressive strength tests. *Metals* **2024**, *14*, 542. [CrossRef]
15. Singh, P.; Shrivastava, V.; Abhash, A.; Yadav, B.N.; Singh, L.B.; Mondal, D.P. Compressive deformation and corrosion behaviour of moderate to highly porous Ti_4Al_4Co (wt%) alloy foam. *Mater. Chem. Phys.* **2021**, *257*, 123718. [CrossRef]
16. Yang, X.; Ma, W.J.; Gu, W.P.; Zhang, Z.Y.; Wang, B.; Wang, Y.; Liu, S. Multi-scale microstructure high-strength titanium alloy lattice structure manufactured via selective laser melting. *RSC Adv.* **2021**, *11*, 22734. [CrossRef]
17. Novak, N.; Al-Ketan, O.; Mauko, A.; Yilmaz, Y.E.; Opara, L.K.; Tanaka, S.; Hokamoto, K.; Rowshan, R.; Al-Rub, R.A.; Vesenjak, M.; et al. Impact loading of additively manufactured metallic stochastic sheet-based cellular material. *Int. J. Impact Eng.* **2023**, *174*, 104527. [CrossRef]
18. Xue, Z.Y.; Hutchinson, J.W. A comparative study of impulse-resistant metal sandwich plates. *Int. J. Impact Eng.* **2004**, *30*, 1283–1305. [CrossRef]
19. Gümrük, R.; Mines, R.A.W. Compressive behaviour of stainless steel micro-lattice structures. *Int. J. Mech. Sci.* **2013**, *68*, 125–139. [CrossRef]
20. Yang, Z.L.; Liu, H.; Wu, Q.; Long, L. Study of energy absorption characteristics and deformation mechanism of stretching–bending synergistic lattices under dynamic compression. *Adv. Eng. Mater.* **2022**, *25*, 2201130. [CrossRef]
21. Fallahi, H.; Sadighi, M.; Samandari, S.S. Compressive mechanical properties of open-cell cubic and rhombic dodecahedron lattice structures of variable cross section fabricated by fused deposition modeling. *Mech. Mater.* **2023**, *184*, 104712. [CrossRef]
22. Ozdemir, Z.; Nava, E.H.; Tyas, A.; Warren, J.A.; Fay, S.D.; Goodall, R.; Todd, I.; Askes, H. Energy absorption in lattice structures in dynamics: Experiments. *Int. J. Impact Eng.* **2016**, *89*, 49–61. [CrossRef]
23. Xiao, L.J.; Song, W.D.; Wang, C.; Tang, H.P.; Fan, Q.B.; Liu, N.; Wang, J.Z. Mechanical properties of open-cell rhombic dodecahedron titanium alloy lattice structure manufactured using electron beam melting under dynamic loading. *Int. J. Impact Eng.* **2017**, *100*, 75–89. [CrossRef]
24. Xiao, L.J.; Song, W.D.; Wang, C.; Tang, H.P.; Fan, Q.B.; Liu, N.; Wang, J.Z. Mechanical behavior of open-cell rhombic dodecahedron Ti–6Al–4V lattice structure. *Mater. Sci. Eng. A* **2015**, *640*, 375–384. [CrossRef]
25. Babaee, S.; Jahromi, B.H.; Ajdari, A.; Nayeb-Hashemi, H.; Vaziri, A. Mechanical properties of open-cell rhombic dodecahedron cellular structures. *Acta Mater.* **2012**, *60*, 2873–2885. [CrossRef]

26. Babamiri, B.B.; Askari, H.; Hazeli, K. Deformation mechanisms and post-yielding behavior of additively manufactured lattice structures. *Mater. Des.* **2020**, *188*, 108443. [CrossRef]
27. Epasto, G.; Palomba, G.; D'Andrea, D.; Bella, D.S.; Mineo, D.R.; Guglielmino, E.; Traina, F. Experimental investigation of rhombic dodecahedron micro-lattice structures manufactured by electron beam melting. *Mater. Today* **2019**, *7*, 578–585. [CrossRef]
28. Yang, L.; Han, C.J.; Wu, H.; Hao, L.; Wei, Q.; Yan, C.; Shi, Y. Insights into unit cell size effect on mechanical responses and energy absorption capability of titanium graded porous structures manufactured by laser powder bed fusion. *J. Mech. Behav. Biomed. Mater.* **2020**, *109*, 103843. [CrossRef]
29. Cao, X.F.; Duan, S.Y.; Liang, J.; Wen, W.B.; Fang, D. Mechanical properties of an improved 3D-printed rhombic dodecahedron stainless steel lattice structure of variable cross section. *Int. J. Mech. Sci.* **2018**, *145*, 53–63. [CrossRef]
30. Cao, X.F.; Duan, S.Y.; Liang, J.; Wen, W.B.; Fang, D. Dynamic compressive behavior of a modified additively manufactured rhombic dodecahedron 316L stainless steel lattice structure. *Thin-Walled Struct.* **2020**, *148*, 106586. [CrossRef]
31. Li, B.Q.; Wang, L.; Li, H.D.; Cui, G.; Su, B.X.; Yao, L.H.; Luo, L.S. Solidification characterization and its correlation with the mechanical properties and functional response of NiTi shape memory alloy manufactured by electron beam freeform fabrication. *Addit. Manuf.* **2021**, *48*, 102468. [CrossRef]
32. Banhart, J.; Baumeister, J.; Weber, M. Damping properties of aluminium foams. *Mater. Sci. Eng. A* **1996**, *205*, 221–228. [CrossRef]
33. Liu, Q.W.; Feng, Y.; Liu, B.C.; Xie, Q.; Zhou, J.J.; Zhang, G.H. Regulation of microstructure, phase transformation behavior, and enhanced high superelastic cycling stability in laser direct energy deposition NiTi shape memory alloys via aging treatment. *Mater. Sci. Eng. A* **2024**, *915*, 147207. [CrossRef]
34. Lu, H.Z.; Liu, L.H.; Yang, C.; Luo, X.; Song, C.H.; Wang, Z.; Wang, J.; Su, Y.D.; Ding, Y.F.; Zhang, L.C.; et al. Simultaneous enhancement of mechanical and shape memory properties by heat-treatment homogenization of Ti_2Ni precipitates in TiNi shape memory alloy fabricated by selective laser melting. *J. Mater. Sci. Technol.* **2022**, *101*, 205–216. [CrossRef]
35. Zhou, X.; Liu, D.; Bu, H.L.; Deng, L.L.; Liu, H.G.; Yuan, P.; Du, P.X.; Song, H.Z. XRD-based quantitative analysis of clay minerals using reference intensity ratios, mineral intensity factors, Rietveld, and full pattern summation methods: A critical review. *Solid Earth Sci.* **2018**, *3*, 16–29. [CrossRef]
36. Zeng, C.Y.; Cao, S.; Li, Y.Y.; Zhao, Z.X.; Zhu, Z.W.; Wang, D.X.; Ma, X.; Zhang, X.P. Two-step constrained aging treatment enabled superior two-way shape memory effect and elevated R-phase transformation temperatures in a rapidly solidified $Ni_{51}Ti_{49}$ alloy. *J. Alloys Compd.* **2019**, *785*, 1180–1188. [CrossRef]
37. Yi, J.C.; Wan, L.; Shu, T.; Zhang, X.W.; Liu, F.; Cheng, G.J. Unleashing multi-scale mechanical enhancement in NiTi shape memory alloy via annular intra-laser deposition with homogenized Ti_2Ni nanoprecipitates. *Acta Mater.* **2024**, *262*, 119418. [CrossRef]
38. Lee, T.J.; Kim, W.J. Effect of severe plastic deformation and post-deformation heat treatment on the microstructure and superelastic properties of $Ti_{50.8}Ni$ alloy. *Materials* **2022**, *15*, 7822. [CrossRef]
39. Toker, G.P.; Saedi, S.; Acar, E.; Ozbulut, O.E.; Karaca, H.E. Loading frequency and temperature dependent damping capacity of NiTiHfPd shape memory alloy. *Mech. Mater.* **2020**, *150*, 103565. [CrossRef]
40. Liu, S.; Zhu, J.; Lin, Y.; Wang, G.C.; Wang, X.B. Effect of stretching-bending deformation and aging treatment on phase transformation behavior and superelasticity of Ti-50.8 at.% Ni alloy. *Intermetallics* **2021**, *129*, 107051. [CrossRef]
41. Pu, Z.; Du, D.; Zhang, D.Q.; Li, Z.X.; Xue, S.; Xi, R.; Wang, X.B.; Chang, B.H. Improvement of tensile superelasticity by aging treatment of NiTi shape memory alloys fabricated by electron beam wire-feed additive manufacturing. *J. Mater. Sci. Technol.* **2023**, *145*, 185–196. [CrossRef]
42. Zhang, M.G.; Li, X.Z.; Wang, B.L.; Jiao, G.H.; Yang, Y.; Fang, X.W.; Huang, K. Prominent superelastic response induced by Ni_4Ti_3 phase in NiTi alloysfabricated via wire-arc directed energy deposition. *Mater. Sci. Eng. A* **2024**, *897*, 146366. [CrossRef]
43. Sugimoto, K.; Mori, T.; Shiode, S. Effect of composition on the internal friction and Young's modulus in γ-phase Mn-Cu alloys. *Met. Sci. J.* **1973**, *7*, 103–108. [CrossRef]
44. Bidaux, J.E.; Schaller, R.; Beniot, W. Study of the h.c.p.-f.c.c. phase transformation in cobalt by acoustic measurements. *Acta Metall.* **1989**, *37*, 803–811. [CrossRef]
45. Engene, B.; Yalçın, B. Experimental investigation on the mechanical properties of Ti6Al4V cellular structures produced with selective laser melting: Effects of rib thickness, unit cell type and orientation. *Proc. Inst. Mech. Eng. Part E J. Process Mech. Eng.* **2024**, 1–12. [CrossRef]
46. Han, D.; Zhang, Y.; Zhang, X.Y.; Xie, Y.M.; Ren, X. Lightweight auxetic tubular metamaterials: Design and mechanical characteristics. *Compos. Struct.* **2023**, *311*, 116849. [CrossRef]
47. Liu, H.Z.; Ma, H.W.; Cai, W.S.; Luo, X.; Wang, Z.; Song, C.H.; Yin, S.; Yang, C. Stable tensile recovery strain induced by a Ni_4Ti_3 nanoprecipitate in a $Ni_{50.4}Ti_{49.6}$ shape memory alloy fabricated via selective laser melting. *Acta Mater.* **2021**, *219*, 117261. [CrossRef]

48. Xu, J.L.; Bao, L.Z.; Liu, A.H.; Jin, X.F.; Luo, J.M.; Zhong, Z.C.; Zheng, Y.F. Effect of pore sizes on the microstructure and properties of the biomedical porous Ni-Ti SMAs prepared by microwave sintering. *J. Alloys Compd.* **2015**, *645*, 137–142. [CrossRef]
49. Costanza, G.; Tata, M.E.; Libertini, R. Effect of temperature on the mechanical behavior of Ni-Ti shape memory sheets. In *TMS2016 Annual Meeting Supplemental Proceedings*; TMS, Ed.; The Minerals, Metals & Materials Society: Pittsburgh, PA, USA, 2016.

Disclaimer/Publisher's Note: The statements, opinions and data contained in all publications are solely those of the individual author(s) and contributor(s) and not of MDPI and/or the editor(s). MDPI and/or the editor(s) disclaim responsibility for any injury to people or property resulting from any ideas, methods, instructions or products referred to in the content.